RAPID COMMUNICATIONS

PHYSICAL REVIEW A **00**, 001400(R) (2016)

Diamond-nitrogen-vacancy electronic and nuclear spin-state anticrossings under weak transverse magnetic fields

Hannah Clevenson,[1,2,*] Edward H. Chen,[1,2] Florian Dolde,[1] Carson Teale,[1,2] Dirk Englund,[1,†] and Danielle Braje[2,‡]

[1]*Massachusetts Institute of Technology, Cambridge, Massachusetts 02139, USA*

[2]*MIT Lincoln Laboratory, Lexington, Massachusetts 02420, USA*

(Received 22 February 2016; published xxxxxx)

We report on detailed studies of electronic and nuclear spin states in the diamond-nitrogen-vacancy (NV) center under weak transverse magnetic fields. We numerically predict and experimentally verify a previously unobserved NV hyperfine level anticrossing (LAC) occurring at bias fields of tens of gauss—two orders of magnitude lower than previously reported LACs at ∼500 and ∼1000 G axial magnetic fields. We then discuss how the NV ground-state Hamiltonian can be manipulated in this regime to tailor the NV's sensitivity to environmental factors and to map into the nuclear spin state.

DOI: 10.1103/PhysRevA.00.001400

Nitrogen-vacancy (NV) defect centers in diamond are optically polarizable quantum systems with spin-dependent fluorescence. Using electron spin resonance (ESR) under ambient conditions, sensitivity to electric fields [1–4], transverse and axial magnetic fields [5–10], temperature [11–14], strain [15], and pressure [16] have been observed via resonance frequency shifts of the NV ground-state manifold. Nonseparable sensitivity to multiple environmental factors is problematic when it comes to using the NV as a sensor. However, the Hamiltonian governing the measurable frequency shifts can be tailored to enhance (or to suppress) sensitivity to different physical phenomena. A magnetic bias field applied parallel or perpendicular [$B_{||}$ or $B_{\perp}$ as shown in Fig. 1(a)] to the NV's axis in the diamond crystal lattice energetically separates the spin states and increases sensitivity to magnetic or electric fields, respectively.

In this Rapid Communication, we investigate an unexplored weak-field regime in which electronic spin ground-state energy level splittings are on par with the Zeeman shift induced by an applied magnetic field. Here we account for both the electron and the nuclear spin of the NV, which reveals complex dynamics of nuclear spin state degeneracy and previously unobserved hyperfine level anticrossings. These features occur at a low magnetic field ($B_{\perp} \lesssim 40$ G) as compared to the $B_{||} \sim 500$ and $B_{||} \sim 1000$ G excited- and ground-state crossings [17–20], which have been used for nuclear spin polarization, providing increased sensitivity to resonance shifts through narrower effective linewidth and increased contrast [21–24]. We find excellent agreement between experiment and theory and discuss the utility of the nuclear spin degeneracy regime toward NV sensing applications and solid-state atomic memories based on nuclear spin polarization. While the results described here are specific to the NV, similar anticrossings are expected in any spin-1 (or higher) defect center that shows hyperfine level splitting on the same order of magnitude as double-electron spin flip anticrossings.

The NV is a two-site defect with a spin-1 electronic ground state, which is magnetically coupled to nearby nuclear spins. For a single NV orientation, energy level shifts are described by the following spin Hamiltonian of the ground triplet state in the presence of magnetic, electric, and strain fields [25], taking into account the zero-field splitting, nuclear and electronic Zeeman shifts, Stark shifts, hyperfine splitting, and nuclear quadrupole effects:

$$\begin{aligned}\mathcal{H}_{gs} = {} & (hD_{gs} + d_{||}\Pi_z)\left[S_z^2 - \frac{1}{3}S(S+1)\right] \\ & - d_{\perp}\left[\Pi_x\left(S_x^2 - S_y^2\right) + \Pi_y(S_xS_y + S_yS_x)\right] \\ & + \mu_B g_e(\vec{S}\cdot\vec{B}) - \mu_n g_n(\vec{B}\cdot\vec{I}) \\ & + A_{||}S_zI_z + A_{\perp}(S_xI_x + S_yI_y) + P_{gs}\left(I_z^2 - \frac{I^2}{3}\right),\end{aligned} \tag{1}$$

where hD_{gs} is the NV ground-state crystal field splitting energy (which is temperature-dependent [14]), $d_{\perp}$ and $d_{||}$ are the components of the ground-state electric dipole moment, the total effective electric field $\vec{\Pi} = \vec{E} + \vec{\sigma}$ encompasses both static electric fields $\vec{E}$ and strain $\vec{\sigma}$, g_e and g_n are the electric and nuclear Landé g factors, μ_B and μ_n are the Bohr and nuclear magneton constants, $\vec{B}$ is the applied magnetic field, $A_{||}$ and $A_{\perp}$ describe the axial and transverse magnetic hyperfine interactions with the ^{14}N nucleus, P_{gs} is the nuclear electric quadrupole parameter, $\vec{S}$ is the electron spin operator, and $\vec{I}$ is the spin operator of the ^{14}N nucleus.

Figure 1 shows the numerically calculated electronic ground-state triplet and ^{14}N hyperfine energy levels $|m_s,m_I\rangle$, where m_s is the electronic spin state and m_I is the nuclear spin state, as a function of the axial magnetic field for a fixed transverse magnetic field. State-mixing-induced anticrossings are seen when the dressed states (black lines) do not follow high-axial field eigenstates (solid and dashed colored lines). With the addition of a weak (<3 G) axial magnetic field, we see mixing and crossing of the energy levels, resulting from off-diagonal terms in $\mathcal{H}_{gs}$ in the $|m_s,m_I\rangle$ basis. The double-electron spin flip anticrossings occur as the nondressed $m_s = 1$ states cross $m_s = -1$ states with identical nuclear spin, for example, as $|1,0\rangle$ crosses $|-1,0\rangle$. The transverse magnetic field leads to second-order mixing of the $m_s = \pm 1$ states; therefore the coupling strength E_g of these electronic Zeeman

*hannahac@mit.edu
†englund@mit.edu
‡braje@ll.mit.edu

 ©2016 American Physical Society

The Lincoln Laboratory portion of this work is sponsored by the Assistant Secretary of Defense for Research & Engineering under Air Force Contract #FA8721-05-C-0002. Opinions, interpretations, conclusions and recommendations are those of the authors and are not necessarily endorsed by the United States Government.

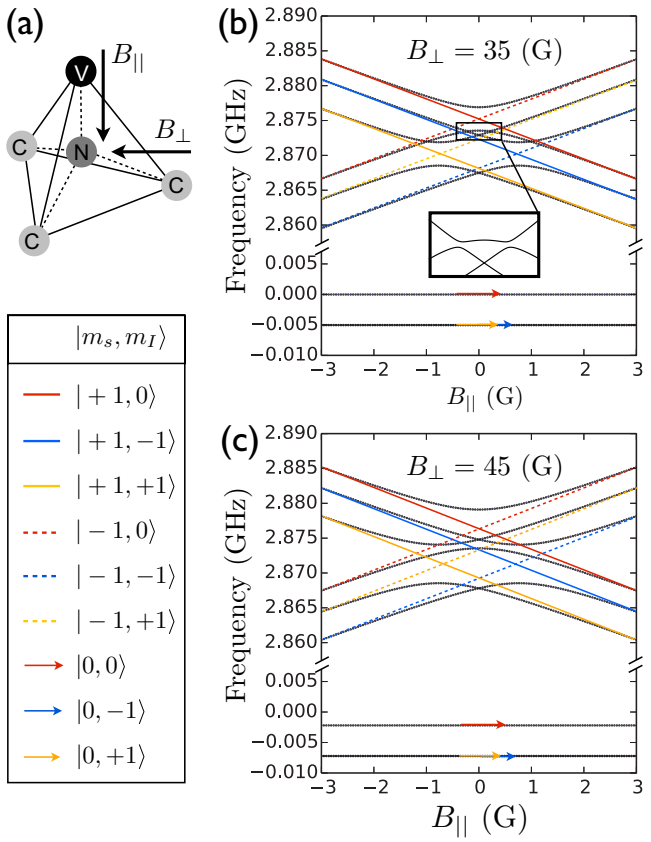


FIG. 1. (a) Axial and transverse magnetic field directions with respect to the NV axis. As $B_\perp$ is increased from (b) 35 to (c) 45 G, the $m_I = 0$ energy levels are separated from the $m_I = \pm 1$ energy levels, removing the degeneracy which results in an electron-nuclear spin flip anticrossing, which is detailed in the inset of (b). Nondressed states are indicated with colored lines and dressed states are indicated with black lines.

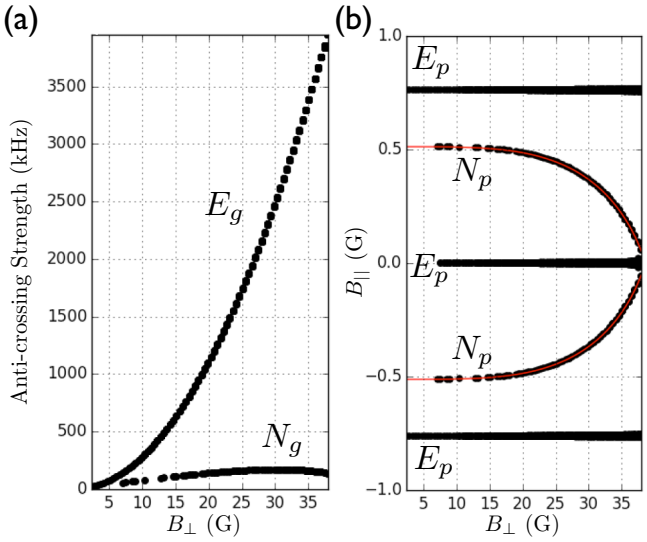


FIG. 2. (a) Anticrossing coupling strength with increasing $B_\perp$. (b) Magnitude of small axial B fields at which the centers of these anticrossings are observed. In both plots, the double-electron spin flip anticrossing is marked E and the electron-nuclear spin flip anticrossing is marked N. At fields greater than $B_\perp \sim 40$ G, anticrossing E continues to increase quadratically and anticrossing N goes to zero as the energy levels no longer overlap.

interaction driven level anticrossings scales quadratically with respect to the applied transverse magnetic field as described in [25].

For transverse magnetic fields under ~40 G, as shown in Fig. 1(b), an additional level anticrossing arises. As this phenomena has not been previously described, to our knowledge, we investigate it here in greater detail. The dressed $m_I = 0$ levels (black lines roughly following the red dashed and solid lines) cross the dressed $m_I = \pm 1$ levels (black lines roughly following the blue and yellow dashed and solid lines), resulting in further state mixing and an electron-nuclear spin flip anticrossing. Solving for the eigenstates of $\mathcal{H}_{gs}$ indicates that transverse magnetic fields induce state mixing in the low axial magnetic field regime by bringing the nuclear spin states into resonance via the electronic Zeeman term $[\mu_B g_e(\vec{S}\cdot\vec{B})]$ in the presence of the transverse hyperfine interaction $[A_\perp(S_x I_x + S_y I_y)]$. This state-mixing results in dressed states and affects which transitions are allowed by optical transition selection rules. As only electron-spin flips (S_x and S_y operators) are considered in our calculation, the nuclear spin flip results from driving the electron spin flip. This is a spin-preserving process. For transverse magnetic fields larger than ~40 G, the energy separation added by the transverse magnetic field removes the $m_I = 0, m_I = \pm 1$ level degeneracy; therefore, this additional anticrossing is no longer present, leaving only the double-electron spin flip anticrossing, which is not mediated by the hyperfine interaction.

Figure 2 depicts the double-electron spin flip and electron-nuclear spin flip anticrossing coupling strengths (E_g, N_g) and the axial magnetic field positions (E_p, N_p) of these anticrossings as a function of the transverse magnetic field. As predicted in Ref. [25], the coupling strength of the double-electron spin flip anticrossing is proportional to the applied transverse magnetic field squared: $E_g \simeq (\mu_B g_e B_\perp)^2/(D_{gs} + d_{||}\Pi_z)$ in the weak electric field, weak axial magnetic field regime. These electron-spin anticrossings are centered around $E_p = 0, \pm A_{||}h/g_e\mu_B$. While E_g continues to increase as $B_\perp$ increases, N_g disappears at $B_\perp \sim 40$ G when the energy levels no longer overlap. The axial magnetic field position about which this anticrossing is centered (N_p) goes to zero with increasing $B_\perp$ (see App. A).

We experimentally validate this anticrossing by performing ESR measurements on an NV ensemble. The epitaxially grown diamond is polished to trap the green pump light and guide the red spin-dependent fluorescence to a photodetector in a light-trapping diamond waveguide geometry [26]. We estimate the intrinsic strain in this sample to be $\sim 3 \times 10^{-5}$ from the ~600 kHz strain splitting of the central hyperfine resonance at zero applied field, given values of $d_\perp$ from the literature [27]. We expect this to be the average strain experienced across the sample. The NV has four orientations in the diamond lattice, labeled as $k = 1,2,3,4$ as seen in Fig. 3(b). We lift the $m_s = \pm 1$ degeneracy and the orientation degeneracy by applying a static magnetic field at an angle resulting in nonequivalent

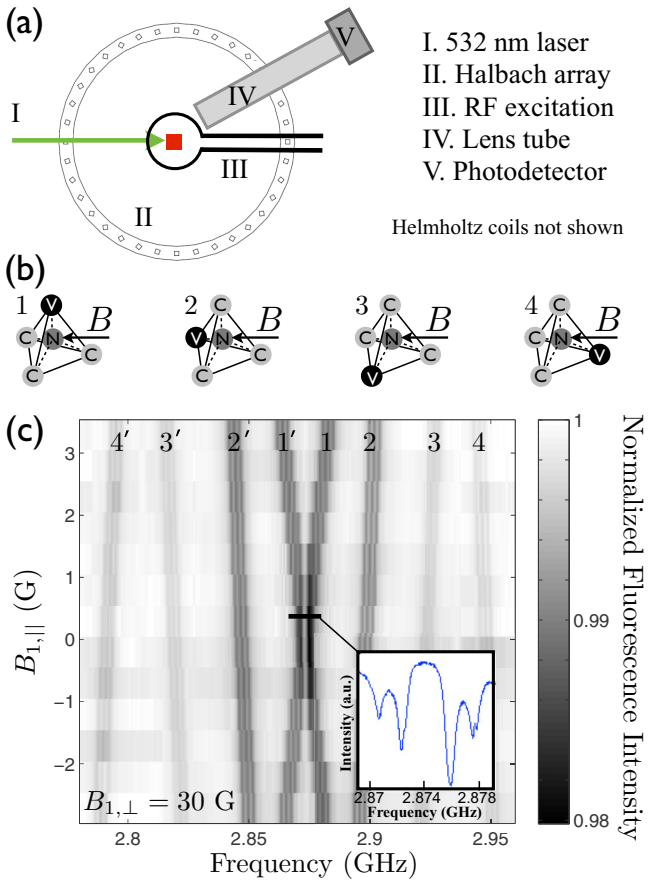


FIG. 3. (a) Experimental setup. (b) The four orientation subensembles of NV centers are shown with an applied magnetic field. (c) An anticrossing strength of ∼2.6 MHz is seen in subensemble 1 when the perpendicular component of the B field ($B_{1,\perp}$) is equal to 30 G and the axial component of the B field ($B_{1,||}$) is varied around zero field. Inset shows a high resolution spectra of resonance 1 and 1′.

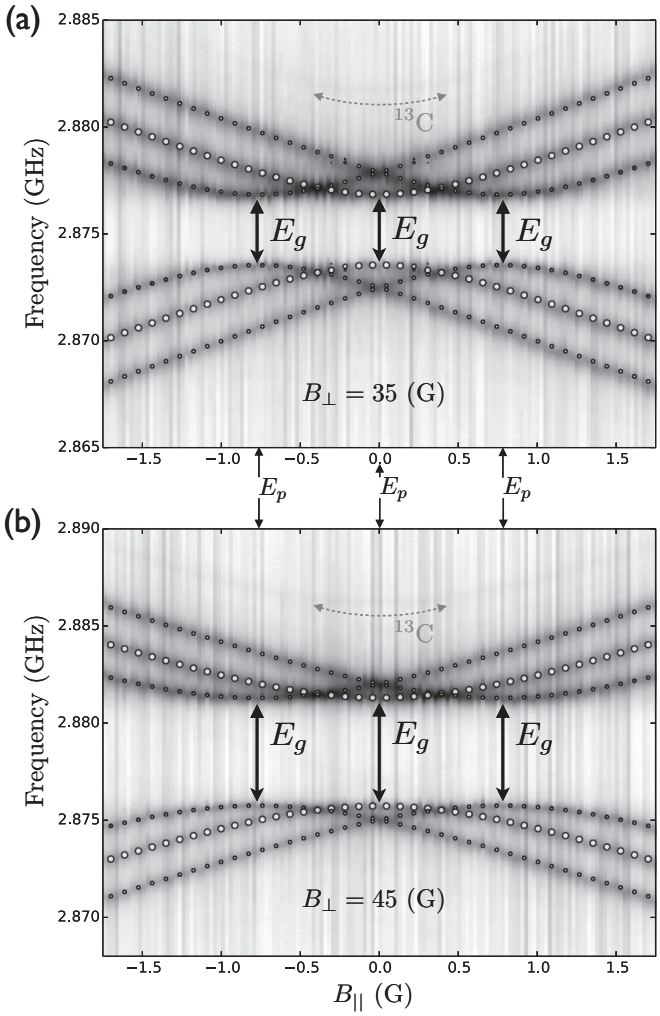


FIG. 4. Plots of transition energies as a function of the axial magnetic field under fixed transverse magnetic fields. Transitions for $B_\perp = 35$ and $B_\perp = 45$ G are shown, which correspond to the energy levels in Fig. 1. Grayscale indicates normalized fluorescence. Double-electron spin anticrossings of coupling strength E_g are seen at $E_p = 0, \pm A_{||}h/g_e\mu_B \simeq \pm 0.75$ G. ESR in diamond with a natural abundance of carbon isotopes has additional resonances due to hyperfine interactions with the ∼1% ($I = 1/2$) ^{13}C nuclear spins; these features are visible at correspondingly lower contrast in both (a) and (b), the highest contrast of which is labeled.

projections onto each orientation. A 60 G Halbach array (magnitude uniformity >99% over a 2 cm^3 volume at the center) is positioned around the sample [Fig. 3(a)] to provide this static magnetic field. In addition, up to ±30 G can be applied in $\hat{X}$, $\hat{Y}$, or $\hat{Z}$ (lab frame) using Helmholtz coils. The total magnetic field is aligned to be perpendicular to the $k = 1$ orientation. A weak axial magnetic field sweep ($B_{1,||}$) in addition to this transverse field confirms the anticrossings in the ESR spectra [Fig. 3(c)]. Each NV orientation produces two Zeeman-split triplets, corresponding to the hyperfine coupling of the ^{14}N nuclear spins. These pairs are located symmetrically around $\omega_c = D_{gs} + \frac{3\mu_B^2 g_e^2}{2\hbar^2 D_{gs}} B_\perp^2$. In levels 1 and 1′, for which the magnetic field is perpendicular, we observe both predicted anticrossings around $B_{1,||} = N_p$. This is highlighted in the inset to Fig. 3(c).

While Fig. 1 gives insight into the origin of the level anticrossings in the energy level diagram, Fig. 4 shows the corresponding energy level transitions at $B_\perp = 35$ and 45 G. Numerical solutions to $\mathcal{H}_{gs}$ accounting for S_x and S_y operators in the selection rules are plotted in conjunction with the experimental data. For both values of the transverse field, we clearly see double-electron spin flip anticrossings centered at $B_{||} = 0, \pm A_{||}h/g_e\mu_B$ G [Fig. 2(b)] with anticrossing coupling strengths corresponding to those expected from Fig. 2(a). As expected, we also see the center frequency between the split resonances increase with increased applied transverse magnetic field.

Figure 5 concentrates on the region of interest at $B_{1,\perp} = 30$ G around which the electron-nuclear spin flip anticrossing is maximized. We observe the electron-nuclear spin flip anticrossing at $\sim \pm 0.35$ G applied axial magnetic field as predicted by analytically solving $\mathcal{H}_{gs}$ (see App. A). Double-electron spin flip anticrossings are centered at $E_p = 0, \pm A_{||}h/g_e\mu_B$ [Fig. 2(b)] with anticrossing coupling strengths corresponding to those predicted by simulation and

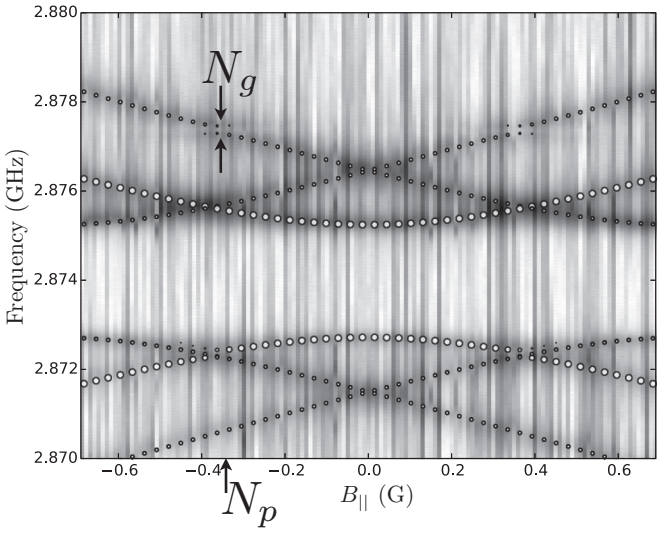


FIG. 5. Detail of double-electron and electron-nuclear spin anticrossings at $B_\perp = 30$ G, where grayscale represents normalized fluorescence. The rf excitation power was reduced by 10 dB to reduce power broadening. This allows the higher-resolution features to be observed; however it is at the expense of the signal-to-noise ratio. Electron-nuclear spin anticrossings of coupling strength $N_g \simeq 250$ kHz are seen centered around $N_p \simeq \pm 0.35$ G, separated in frequency by P_{gs} at 2.877 and 2.872 GHz. Numerical solutions to $\mathcal{H}_{gs}$ are plotted over the data, with the diameter of the circles corresponding to the probability of the transition.

plotted in Fig. 2(a). Note the excellent agreement between the experiment and the theoretical model.

The numerical simulation of $\mathcal{H}_{gs}$ in the $\lesssim$40 G transverse-field regime gives insight into the level structure and the region where the crossings and anticrossings can be seen; here we describe several useful applications in sensing and atomic memories. First, the double-electron spin anticrossing addresses the ever-present challenge of isolating sensitivity to multiple fields by suppressing sensitivity to changes in axial magnetic fields. As the applied transverse magnetic field is increased, the strength of this anticrossing increases quadratically, and the range of $B_{||}$ to which the NV ensemble is insensitive increases [2]; this is especially useful for electric field and temperature sensing, where the effects of magnetic fields can limit sensitivity.

Second, the double-electron spin anticrossing causes two of the three hyperfine transition levels to cross. At these degeneracies, ESR spectra experience doubled signal contrast. In cw diamond-based sensing applications, where sensitivity is linearly proportional to the ESR resonance contrast, twice the sensitivity is expected in this regime. Furthermore, as this anticrossing strength increases and the hyperfine transition levels are compressed in energy spacing, all three nuclear levels can be effectively degenerate, providing up to a factor of 3 increase in sensitivity to electric fields or temperature. Up until now, we have shown experimental-theoretical agreement for the six hyperfine transitions present in a ^{14}N sample, where the nuclear spin $I_{^{14}N} = 1$. Note that the four transitions present in ^{15}N allow for a complete nuclear spin degeneracy at zero applied axial magnetic field (see App. B).

Next, we propose a transverse magnetic field regime method to remove temperature sensitivity from diamond-based magnetometry measurements. Taking the derivative of ω_c with respect to temperature, the temperature-dependent D_{gs} term in the denominator of the second order term leads to a decrease in $d\omega_c/dT$ with increased transverse magnetic field [14]. We expect a 1% decrease in $d\omega_c/dT$ with an 80 G applied transverse magnetic field. Combining this advantage with the aforementioned increase in contrast and insensitivity to changes in B_z in a high signal-to-noise-ratio light-trapping diamond waveguide results in a regime that is well suited for temperature-stabilized measurements, relying on the ability to probe multiple subensembles with different crystallographic projections of the applied transverse magnetic field. Synchronizing the ratio of the resonance frequencies of subensembles with known, varying dependences on temperature allows the temperature dependence to be stabilized, similar to the method proposed by Hodges *et al.* using strain engineering [28]. This method further decouples the diamond from its thermal environment, addressing an ongoing challenge in diamond-based electric and magnetic field sensing.

Finally, using these low-transverse-field anticrossings, we introduce an alternate route to polarize the nuclear spin host of the nitrogen-vacancy center [21,29–32]. This method articulates successive shifting of the magnetic field and radio-frequency pulses iteratively to transfer the spin polarization into a single nuclear state, similar to methods explored for optical quantum dots [33–35]. Unlike existing schemes at ∼500 and ∼1000 G axial magnetic fields for the excited state and ground-state level anticrossings (LACs), this approach relies on the control of weak magnetic fields and state-selective rf pulses. It requires fewer pulses and a smaller range of rf excitation than other low-magnetic field recursively repeated protocols [36]. The heart of the scheme relies on adiabatic passage, which results in a change in the nuclear spin state. Following Landau-Zener-Stueckelberg theory [37–39], the probability P of adiabatic passage through an anticrossing with coupling strength Δ is $P = 1 - e^{(-\pi h \Delta^2/2\frac{d\Lambda}{dt})}$ where $\frac{d\Lambda}{dt}$ is the rate of change of the energy difference as the gap is approached. Under these conditions, sweeping a bias field through the $\pm B_{||} = N_p$ electron-nuclear spin flip anticrossing results in spin exchange from $|m_s = \mp 1, m_I = \pm 1\rangle$ to $|m_s = \pm 1, m_I = 0\rangle$. For a 99.99% probability of adiabatic passage, a rate of magnetic field change of 1 G/225 μs is required.

While many nuclear spin exchange sequences are possible, here we note a two-step example to polarize into $m_I = 0$. Assuming an initial ensemble of NVs in a mixture of eigenstates $|0,-1\rangle$, $|1,1\rangle$, and $|1,0\rangle$, which can be prepared through state-selective excitations, a single application of the protocol results in a mixture of eigenstates $|0,-1\rangle$, $|1,0\rangle$, and $|-1,0\rangle$. The population transferred through the electron-nuclear spin flip anticrossing is then shelved in $m_s = 0$ and the remaining population in $|0,-1\rangle$ is transferred to $|-1,-1\rangle$ with a resonant rf pulse. The second application of the protocol then results in eigenstates $|-1,0\rangle$, $|0,0\rangle$, and $|1,0\rangle$. Exploiting the robustness of the nuclear spin state against the optical excitation of the NV, all m_s levels can be pumped into the $m_s = 0$ with green laser excitation [40]. This type of protocol would be useful both for sensing applications, due to the increased contrast, but also for applications like diamond-

based gyroscopes [41,42] and atomic memories [32,43,44], which utilize the longer-lived nuclear spin state.

Additionally, the transverse magnetic fields may help overcome the influence of inhomogeneous strain present from diamond growth processes, a challenge in working with very large ensembles of NV centers. Combining this with insensitivity to small axial magnetic fields and potential insensitivity to temperature, the resultant system also presents itself as a strong candidate for a quantum memory. Transverse and axial magnetic fields could be used to read and write to the system, which is otherwise isolated from its environment.

In conclusion, in this Rapid Communication we present a careful study of the effect of weak transverse magnetic fields on the NV system. We predict and experimentally verify an electron-nuclear spin anticrossing, with close agreement between theory and experiment. We also experimentally measure the predicted double-electron spin anticrossing under transverse magnetic fields. These anticrossings show potential for a variety of sensing applications because of (i) increased signal contrast, (ii) insensitivity to axial magnetic fields near the anticrossing points, (iii) potential for nuclear spin polarization schemes, and (iv) selective decoupling of the NV from its environment through the synchronization of different orientations with varying transverse fields. With applied transverse magnetic fields on the order of tens of gauss, we can achieve increases in contrast on the order of those seen previously only at the much higher, axially applied ∼500 and ∼1000 G LACs.

The authors would like to thank L. Pham, M. E. Trusheim, C. McNally, and T. Schröder for helpful discussions. The Lincoln Laboratory portion of this work is sponsored by the Assistant Secretary of Defense for Research & Engineering under Air Force Contract #FA8721-05-C-0002. Opinions, interpretations, conclusions, and recommendations are those of the authors and are not necessarily endorsed by the United States Government. D.E. acknowledges support from ONR (N00014-13-1-0316). H.C. and E.H.C. are supported by the NASA Office of the Chief Technologist's Space Technology Research Fellowship.

APPENDIX A: ANALYTICAL EXPRESSION FOR THE LOCATION OF AN ELECTRON-NUCLEAR SPIN FLIP ANTICROSSING

Using second order degenerate perturbation theory, we calculate the change in energy as a function of applied magnetic and electric and/or strain fields. By solving for the axial magnetic field $B_{||}$ at which the intersection of the $|m_I = 0\rangle$ and the $|m_I = 1\rangle$ energy levels occurs, we show a closed-form solution for the location of the electron-nuclear spin flip level anticrossing. This is in good agreement with our numerical and experimental observations as seen in Fig. 2.

$$N_p = \frac{-A_\parallel D_{gs}\xi + |P_{gs}|\sqrt{\xi\left(D_{gs}^2\xi + B_\perp^4\right)}}{2D_{gs}\xi} \qquad \text{(A1)}$$

where $\xi = A_\parallel^2 - P_{gs}^2$, $A_\parallel$ is the axial hyperfine interaction, D_{gs} the crystal field splitting, P_{gs} the quadrupole energy, and $B_\perp$ the transverse component of the magnetic field in the NV frame of reference. Figure 5 depicts this transverse field regime. Numerical solutions to $\mathcal{H}_{gs}$ accounting for selection rules are shown in conjunction with experimental data. For questions or comments on this calculation and the numerical simulations, please contact E.H.C. at ehchen@mit.edu.

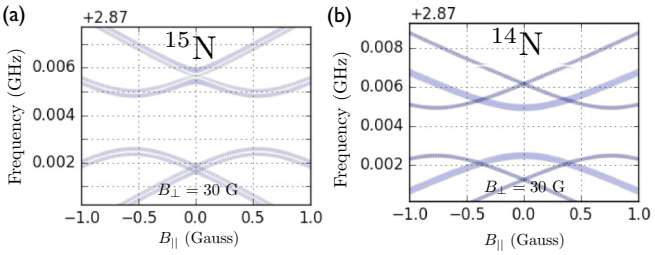


FIG. 6. Comparison of (a) ^{15}N and (b) ^{14}N samples at $B_\perp = 30$ G.

APPENDIX B: IMPLEMENTATION WITH ^{15}N

Unlike ^{14}N, which is a spin-1 system, ^{15}N is a spin-1/2 system. The hyperfine splitting of the NV center would therefore result in two resonances ($\pm 1/2$) instead of three (0, ± 1). This gives a 50% increase in contrast, which is linearly proportional to sensor sensitivity. Furthermore, at zero applied axial magnetic field ($B_{||} = 0$) full contrast is achieved, even at low applied transverse magnetic fields. The electron-nuclear spin anticrossing is not present in the ^{15}N case. Under a transverse magnetic field, the two nuclear spin states become mixed. Therefore the application of a linearly polarized microwave field induces transitions between all (2×2) possible mixed states, giving rise to the doublets of the ODMR spectrum in Fig. 6(a).

[1] F. Dolde, H. Fedder, M. W. Doherty, T. Nobauer, F. Rempp, G. Balasubramanian, T. Wolf, F. Reinhard, L. C. L. Hollenberg, F. Jelezko, and J. Wrachtrup, Nat. Phys. **7**, 459 (2011).

[2] F. Dolde, M. W. Doherty, J. Michl, I. Jakobi, B. Naydenov, S. Pezzagna, J. Meijer, P. Neumann, F. Jelezko, N. B. Manson, and J. Wrachtrup, Phys. Rev. Lett. **112**, 097603 (2014).

[3] M. W. Doherty, J. Michl, F. Dolde, I. Jakobi, P. Neumann, N. B. Manson, and J. Wrachtrup, New J. Phys. **16**, 063067 (2014).

[4] E. V. Oort and M. Glasbeek, Chem. Phys. Lett. **168**, 529 (1990).

[5] D. Budker and M. Romalis, Nat. Phys. **3**, 227 (2007).

[6] J. M. Taylor, P. Cappellaro, L. Childress, L. Jiang, D. Budker, P. R. Hemmer, A. Yacoby, R. Walsworth, and M. D. Lukin, Nat. Phys. **4**, 810 (2008).

[7] J. R. Maze, P. L. Stanwix, J. S. Hodges, S. Hong, J. M. Taylor, P. Cappellaro, L. Jiang, M. V. G. Dutt, E. Togan, A. S. Zibrov, A. Yacoby, R. L. Walsworth, and M. D. Lukin, Nature (London) **455**, 644 (2008).

[8] G. Balasubramanian, I. Y. Chan, R. Kolesov, M. Al-Hmoud, J. Tisler, C. Shin, C. Kim, A. Wojcik, P. R. Hemmer, A. Krueger, T. Hanke, A. Leitenstorfer, R. Bratschitsch, F. Jelezko, and J. Wrachtrup, Nature (London) **455**, 648 (2008).

[9] K. Fang, V. M. Acosta, C. Santori, Z. Huang, K. M. Itoh, H. Watanabe, S. Shikata, and R. G. Beausoleil, Phys. Rev. Lett. **110**, 130802 (2013).

[10] L. Rondin, J.-P. Tetienne, T. Hingant, J.-F. Roch, P. Maletinsky, and V. Jacques, Rep. Prog. Phys. **77**, 056503 (2014).

[11] G. Kucsko, P. C. Maurer, N. Y. Yao, M. Kubo, H. J. Noh, P. K. Lo, H. Park, and M. D. Lukin, Nature (London) **500**, 54 (2013).

[12] D. M. Toyli, F. Charles, D. J. Christle, V. V. Dobrovitski, and D. D. Awschalom, Proc. Natl. Acad. Sci. U.S.A. **110**, 8417 (2013).

[13] P. Neumann, I. Jakobi, F. Dolde, C. Burk, R. Reuter, G. Waldherr, J. Honert, T. Wolf, A. Brunner, J. H. Shim, D. Suter, H. Sumiya, J. Isoya, and J. Wrachtrup, Nano Lett. **13**, 2738 (2013).

[14] M. W. Doherty, V. M. Acosta, A. Jarmola, M. S. J. Barson, N. B. Manson, D. Budker, and L. C. L. Hollenberg, Phys. Rev. B **90**, 041201 (2014).

[15] P. Ovartchaiyapong, K. W. Lee, B. A. Myers, and A. C. B. Jayich, Nat. Commun. **5** (2014). **13**

[16] M. W. Doherty, V. V. Struzhkin, D. A. Simpson, L. P. McGuinness, Y. Meng, A. Stacey, T. J. Karle, R. J. Hemley, N. B. Manson, L. C. L. Hollenberg, and S. Prawer, Phys. Rev. Lett. **112**, 047601 (2014).

[17] R. J. Epstein, F. M. Mendoza, Y. K. Kato, and D. D. Awschalom, Nat. Phys. **1**, 94 (2005).

[18] P. Neumann, R. Kolesov, V. Jacques, J. Beck, J. Tisler, A. Batalov, L. Rogers, N. B. Manson, G. Balasubramanian, F. Jelezko, and J. Wrachtrup, New J. Phys. **11**, 013017 (2009).

[19] G. D. Fuchs, V. V. Dobrovitski, R. Hanson, A. Batra, C. D. Weis, T. Schenkel, and D. D. Awschalom, Phys. Rev. Lett. **101**, 117601 (2008).

[20] R. Fischer, A. Jarmola, P. Kehayias, and D. Budker, Phys. Rev. B **87**, 125207 (2013).

[21] V. Jacques, P. Neumann, J. Beck, M. Markham, D. Twitchen, J. Meijer, F. Kaiser, G. Balasubramanian, F. Jelezko, and J. Wrachtrup, Phys. Rev. Lett. **102**, 057403 (2009).

[22] A. Dréau, M. Lesik, L. Rondin, P. Spinicelli, O. Arcizet, J.-F. Roch, and V. Jacques, Phys. Rev. B **84**, 195204 (2011).

[23] M. Steiner, P. Neumann, J. Beck, F. Jelezko, and J. Wrachtrup, Phys. Rev. B **81**, 035205 (2010).

[24] B. Smeltzer, J. McIntyre, and L. Childress, Phys. Rev. A **80**, 050302 (2009).

[25] M. W. Doherty, F. Dolde, H. Fedder, F. Jelezko, J. Wrachtrup, N. B. Manson, and L. C. L. Hollenberg, Phys. Rev. B **85**, 205203 (2012).

[26] H. Clevenson, M. E. Trusheim, C. Teale, T. Schroder, D. Braje, and D. Englund, Nat. Phys. **11**, 393 (2015).

[27] J. Teissier, A. Barfuss, P. Appel, E. Neu, and P. Maletinsky, Phys. Rev. Lett. **113**, 020503 (2014).

[28] J. S. Hodges, N. Y. Yao, D. Maclaurin, C. Rastogi, M. D. Lukin, and D. Englund, Phys. Rev. A **87**, 032118 (2013).

[29] R. Fischer, C. O. Bretschneider, P. London, D. Budker, D. Gershoni, and L. Frydman, Phys. Rev. Lett. **111**, 057601 (2013). **14**

[30] H.-J. Wang, C. S. Shin, C. E. Avalos, S. J. Seltzer, D. Budker, A. Pines, and V. S. Bajaj, Nat. Commun. **4**, 1940 (2013). **Q**

[31] J. Scheuer, I. Schwartz, Q. Chen, D. Schulze-Sünninghausen, P. Carl, P. Höfer, A. Retzker, H. Sumiya, J. Isoya, B. Luy, M. B. Plenio, B. Naydenov, and F. Jelezko, New J. Phys. **18**, 013040 (2016).

[32] G. D. Fuchs, G. Burkard, P. V. Klimov, and D. D. Awschalom, Nat. Phys. **7**, 789 (2011).

[33] J. M. Nichol, S. P. Harvey, M. D. Shulman, A. Pal, V. Umansky, E. I. Rashba, B. I. Halperin, and A. Yacoby, Nat. Commun. **6** 7682 (2015).

[34] H. Ribeiro and G. Burkard, Phys. Rev. Lett. **102**, 216802 (2009).

[35] P. Nalbach, J. Knörzer, and S. Ludwig, Phys. Rev. B **87**, 165425 (2013).

[36] D. Pagliero, A. Laraoui, J. D. Henshaw, and C. A. Meriles, Appl. Phys. Lett. **105**, 242402 (2014).

[37] L. Landau, Phys. Z. Sowjetunion **2**, 46 (1932). **Q**

[38] C. Zener, Proc. R. Soc. London, Ser. A **137**, 696 (1932).

[39] E. Stuckelberg, Helv. Phys. Acta **5**, 36 (1932). **Q**

[40] P. Neumann, J. Beck, M. Steiner, F. Rempp, H. Fedder, P. R. Hemmer, J. Wrachtrup, and F. Jelezko, Science **329**, 542 (2010).

[41] A. Ajoy and P. Cappellaro, Phys. Rev. A **86**, 062104 (2012).

[42] M. P. Ledbetter, K. Jensen, R. Fischer, A. Jarmola, and D. Budker, Phys. Rev. A **86**, 052116 (2012).

[43] P. C. Maurer, G. Kucsko, C. Latta, L. Jiang, N. Y. Yao, S. D. Bennett, F. Pastawski, D. Hunger, N. Chisholm, M. Markham, D. J. Twitchen, J. I. Cirac, and M. D. Lukin, Science **336**, 1283 (2012).

[44] J. H. Shim, I. Niemeyer, J. Zhang, and D. Suter, Phys. Rev. A **87**, 012301 (2013).